INTERNATIONAL JOURNAL FOR NUMERICAL METHODS IN ENGINEERING
Int. J. Numer. Meth. Engng 2007; **72**:1192–1218

A non-linear programming method approach for upper bound limit analysis

M. Vicente da Silva*,† and A. N. Antão

Departamento de Engenharia Civil, Faculdade de Ciências e Tecnologia, Universidade Nova de Lisboa, Quinta da Torre, Monte da Caparica 2829-516, Portugal

SUMMARY

This paper presents a finite element model based on mathematical non-linear programming in order to determine upper bounds of colapse loads of a mechanical structure.

The proposed formulation is derived within a kinematical approach framework, employing two simultaneous and independent field approximations for the velocity and strain rate fields. The augmented Lagrangian is used to establish the compatibility between these two fields. In this model, only continuous velocity fields are used.

Uzawa's minimization algorithm is applied to determine the optimal kinematical field that minimizes the difference between external and dissipated work rate. The use of this technique allows to bypass the complexity of the non-linear aspects of the problem, since non-linearity is addressed as a set of small local subproblems of optimization for each finite element.

The obtained model is quite versatile and suitable for solving a wide range of collapse problems. This paper studies 3D strut-and-tie structures, 2D plane strain/stress and 3D solid problems. Copyright © 2007 John Wiley & Sons, Ltd.

Received 23 May 2006; Revised 19 February 2007; Accepted 27 February 2007

KEY WORDS: limit analysis; upper bound theorem; augmented Lagrangian; non-linear optimization

1. INTRODUCTION

Over the last two decades, the limit analysis research field has observed important advances. By taking advantage of the rapid growth in computer capabilities, new numerical methods have been developed.

The use of formulations based on standard limit analysis theorems presents two important limitations. First of all, they can only be applied with elastic–perfectly plastic materials to

---

*Correspondence to: M. Vicente da Silva, Departamento de Engenharia Civil, Faculdade de Ciências e Tecnologia, Universidade Nova de Lisboa, Quinta da Torre, Monte da Caparica 2829-516, Portugal.

†E-mail: vicente.silva@fct.unl.pt

geometrically linear problems and with monotonic load cases. Secondly, they provide collapse load estimates and, occasionally, the respective failure mechanisms, but cannot predict the structure behaviour during an intermediate state. Nevertheless, these formulations do not display the error accumulation problems associated with the common elasto-plastic incremental analysis techniques and they require significantly less computational costs.

Most of these models address the limit analysis problem as a mathematical programming problem. It is a well-known fact that the plastic behaviour renders the problem intrinsically non-linear. Essentially, two different approaches are adopted to deal with this fact: (i) the use of linearization techniques associated with linear programming algorithms, found, for example, in Sloan and Kleeman [1], Christiansen [2] and Pastor *et al.* [3]; (ii) models based on direct non-linear programming algorithms, such as the works of Zouain *et al.* [4], Christiansen and Andersen [5], Lyamin and Sloan [6, 7], Li and Yu [8], etc.

The present work can be included in this latter group. The proposed model is a strict upper bound limit theorem numerical implementation, using a mixed finite element formulation in which both the velocity and the strain rate fields are independently approximated. The formation of slip lines caused by discontinuities in the velocity field, admitted in the classical plasticity theory, is discarded in this formulation.

This article is divided into five sections. After this brief introduction, in Section 2, we review some basic plasticity concepts and the upper bound limit analysis theorem, which are required for developing the proposed model. The continuity assumption is stated and discussed. Moreover, the adopted yielding criteria are presented. In Section 3, the finite element formulation is derived. In Section 4, several numerical examples are provided to demonstrate the effectiveness and accuracy of the model. These examples can be divided into three distinct problem categories: struts-and-ties (1D elements), 2D plane strain and plane stress and 3D solids. Finally, concluding remarks are presented in Section 5.

2. THEORETICAL BACKGROUND

2.1. Plasticity basics

Let Ω represent a rigid-perfectly plastic body, delimited by a boundary Γ, with two complementary parts, Γ_u and $\Gamma_\sigma : \Gamma = \Gamma_u \cup \Gamma_\sigma \wedge \Gamma_u \cap \Gamma_\sigma = \emptyset$. In the first region, Γ_u, being denoted as the kinematic boundary, the displacement field, u, is fixed

$$u = 0 \quad \text{in } \Gamma_u \tag{1}$$

The remaining part, Γ_σ, represents the static boundary, in which external surface forces, t, are prescribed.

The structure is subject to a given distribution of a set of constant body loads, b, and external surface forces, t, affected by a load multiplier λ ($\lambda \in \mathbb{R}^+$). The problem under consideration consists of finding the load multiplier that leads the structure to its maximum load bearing capacity and to likely failure, i.e. the collapse load multiplier, λ_c.

Assuming, as previously stated, a rigid-perfectly plastic behaviour, means that the stress tensor value, σ, must comply, on the whole domain, with a *yield criterion*, expressed in the following form:

$$f(\sigma) \leqslant 0 \quad \text{in } \Omega \tag{2}$$

Whenever the equality in (2) holds, the material enters a plastic state and plastic flow can occur. Otherwise, the strains remain null and/or constant. Unlike the theory of elasticity, there is no direct relation between plastic strain, ε, and stress tensors, σ, and the total amount of plastic strain is *a priori* undefined and unlimited.

In order to establish the kinematics of the plastic flow, the rule of normality, which defines the plastic strain rate ($\dot{\varepsilon}$) direction, according to the outward normal to the yield surface, $f(\sigma)=0$, is verified and can be expressed as follows:

$$\dot{\varepsilon}(\sigma)=\alpha\frac{\partial f(\sigma)}{\partial\sigma}, \quad \alpha\geqslant 0 \tag{3}$$

The presented rule is denoted as an associated flow rule, given that the yield function is used to define the plastic flow. If the yield surface has a singularity, the direction of the plastic strain rate, at that point, can be defined by any vector pointing away from the surface, as long as it is located within the *cone* formed by all the normal vectors in the neighbourhood of that point

$$\dot{\varepsilon}(\sigma)\in\alpha\partial f(\sigma), \quad \alpha\geqslant 0 \tag{4}$$

This flow rule can be observed as a direct consequence of the *Maximum plastic work postulate* stated by Hill [9]

$$\forall\sigma: f(\sigma)\leqslant 0, \quad \forall\sigma^*: f(\sigma^*)\leqslant 0, \quad (\sigma-\sigma^*):\dot{\varepsilon}(\sigma)\geqslant 0 \tag{5}$$

Mention must be made of the fact that the above principle is fulfilled only by convex yield surfaces.

By definition, the plastic energy dissipation rate is the result of the tensorial contraction

$$\mathscr{D}(\sigma,\dot{\varepsilon})=\sigma:\dot{\varepsilon} \tag{6}$$

By taking into account (2)–(5), the plastic energy dissipation rate can be derived in such a way that it may depend on the plastic strains only [10]. It should be stated that if the yielding surface is not strictly convex, there might be more than one stress state that originates a given plastic strain rate, but the plastic energy dissipation rate will be solely defined in terms of the plastic strain rate.

For rigid-perfectly plastic material, the velocity field does not have to be continuous in the whole domain. Hence, the plastic energy dissipation rate, $\mathscr{D}$, can be written as:

$$\mathscr{D}=\mathscr{D}(\dot{\varepsilon})+\mathscr{D}(\widehat{v}), \quad \dot{\varepsilon}\in\mathscr{C}_c, \quad \widehat{v}\in\mathscr{C}_d \tag{7}$$

in which, henceforth, $\dot{\varepsilon}$ represents the continuous component of the plastic strain only, and $\widehat{v}$ denotes the possible discontinuous component. The $\mathscr{C}_c$ and $\mathscr{C}_d$ spaces are defined in such a way that they implicitly enforce the compliance with the normality flow rule (3)–(4), by confining the strain tensor rate and the velocity discontinuities to those spaces.

2.2. Limit analysis upper bound theorem

Let us now assume $\dot{u}$ to be a *kinematically admissible* velocity field, i.e. a velocity field that satisfies the Dirichlet boundary condition (1) and the domain compatibility equation

$$\dot{\varepsilon}=B\dot{u} \quad \text{in } \Omega \tag{8}$$

where B is the usual differential compatibility operator.

The upper bound theorem of limit analysis can be stated as follows: if, for a kinematically admissible velocity field, the external load work rate

$$W_e = \lambda \left(\int_\Omega b^{\mathrm{T}} \dot{u} \, \mathrm{d}\Omega + \int_{\Gamma_\sigma} t^{\mathrm{T}} \dot{u} \, \mathrm{d}\Gamma \right) \tag{9}$$

is greater or equal to the total internal plastic energy dissipation rate

$$W_d = \int_\Omega \mathscr{D}(\dot{\varepsilon}) \, \mathrm{d}\Omega + \int_{\Gamma_d} \mathscr{D}(\widehat{v}) \, \mathrm{d}\Gamma \tag{10}$$

then, collapse will occur. In expression (10), Γ_d denotes the region in which a velocity field discontinuity occurs. Now, let us assume the functional J to be defined by

$$J = W_d - W_e \tag{11}$$

By taking into account the previous definition, the solution of the following mathematical minimization problem

$$\lambda^* = \min\{\lambda \mid \exists\, \dot{u} \in S : J = 0\} \tag{12}$$

where S represents a subspace of the set of all kinematically admissible velocity fields, K, gives an upper bound of the collapse load multiplier

$$S \subset K \;\Rightarrow\; \lambda^* \geqslant \lambda_c \tag{13}$$

Otherwise, if S represents the complete K space, the exact collapse load multiplier will be obtained

$$S = K \;\Rightarrow\; \lambda^* = \lambda_c \tag{14}$$

2.3. *Continuity assumption*

This work does not allow for discontinuities in the velocity field. As a direct consequence of this assumption, it is no longer possible to guarantee that the exact collapse load multiplier can be reached within an upper bound theorem approach, in accordance with (13).

Nevertheless, in the authors' opinion, this fact does not represent a relevant disadvantage. Indeed, let us consider a given mechanical structure that requires unavoidably discontinuities to form the respective collapse mechanism. From the authors' experience, it is safe to state that in such cases a kinematical numerical model based on continuous velocity fields can still satisfactorily yield accurate upper bound estimates for the collapse load. This means, that, although in the vicinity of the slip lines, where the singularities take place, the solution error can be relevant, this will not affect significantly the overall solution.

2.4. *Yielding criteria and dissipation functions*

In this paper, four common yielding criteria are considered. They are defined below, in the principal stress space, assuming $\sigma_{\mathrm{I}} \geqslant \sigma_{\mathrm{II}} \geqslant \sigma_{\mathrm{III}}$:

- *Tresca*:

$$f(\sigma) = \sigma_{\mathrm{I}} - \sigma_{\mathrm{III}} - \sigma_0 \tag{15}$$

where σ_0 denotes the uniaxial yield stress;

Table I. Plastic energy dissipation rate functions.

Criteria	$\mathscr{D}(\dot{\varepsilon})$	$\dot{\varepsilon} \in \mathscr{C}_c$
Tresca	$\frac{\sigma_0}{2}(\lvert\dot{\varepsilon}_{\mathrm{I}}\rvert + \lvert\dot{\varepsilon}_{\mathrm{II}}\rvert + \lvert\dot{\varepsilon}_{\mathrm{III}}\rvert)$	$\mathrm{tr}(\dot{\varepsilon}) = 0$
von Mises	$k\sqrt{2\,\mathrm{tr}(\dot{\varepsilon}^2)}$	
Mohr–Coulomb	$\frac{c}{\tan\phi}\mathrm{tr}(\dot{\varepsilon})$	$\mathrm{tr}(\dot{\varepsilon}) \geqslant (\lvert\dot{\varepsilon}_{\mathrm{I}}\rvert + \lvert\dot{\varepsilon}_{\mathrm{II}}\rvert + \lvert\dot{\varepsilon}_{\mathrm{III}}\rvert)\sin\phi$
Drucker–Prager		$\mathrm{tr}(\dot{\varepsilon}) \geqslant \sqrt{\frac{2\sin^2\phi}{3+\sin^2\phi}(3\,\mathrm{tr}(\dot{\varepsilon}^2) - \mathrm{tr}^2(\dot{\varepsilon}))}$

- *von Mises*:

$$f(\sigma) = \sqrt{\tfrac{1}{2}\mathrm{tr}(s^2)} - k \tag{16}$$

  where s represents the deviatoric stress, k the pure shear yield stress and $\mathrm{tr}(\cdot)$ denotes the trace tensorial operation;
- *Mohr–Coulomb*:

$$f(\sigma) = \sigma_{\mathrm{I}}(1 + \sin\phi) - \sigma_{\mathrm{III}}(1 - \sin\phi) - 2c\cos\phi \tag{17}$$

  where c represents the cohesion and ϕ the angle of shearing resistance;
- *Drucker–Prager*:

$$f(\sigma) = \sqrt{\frac{1}{2}\mathrm{tr}(s^2)} - \frac{3\sin\phi}{\sqrt{3(3+\sin^2\phi)}}\left(\frac{c}{\tan\phi} - \frac{1}{3}\mathrm{tr}(\sigma)\right) \tag{18}$$

Table I summarizes the internal energy dissipation functions together with the respective $\mathscr{C}_c$ space definition, for all the previously mentioned yielding criteria. These expressions are presented only for the continuous strain rate condition.

3. NUMERICAL FORMULATION

As a starting point, let us divide the domain, Ω, into n_E finite elements. For each element, two independent and simultaneous approximations, for the velocity and plastic strain rate fields, are used

$$\dot{u}_i = \{v_x, v_y, v_z\}_i^{\mathrm{T}} = N_i d_i \qquad \text{in } \Omega_i \tag{19}$$

$$\dot{\varepsilon}_i = \{\dot{\varepsilon}_x, \dot{\varepsilon}_y, \dot{\varepsilon}_z, 2\dot{\varepsilon}_{xy}, 2\dot{\varepsilon}_{yz}, 2\dot{\varepsilon}_{xz}\}_i^{\mathrm{T}} = E_i e_i \qquad \text{in } \Omega_i \tag{20}$$

The matrices N and E collect the approximation functions and the vectors d and e their associated weights, in reference to the ith finite element. For simplicity, the notation used in this section assumes the 3D problem form. The adjustments needed for other types of problems are straightforward.

The velocity approximation functions used are the conventional *nodal shape functions* from the finite element method, FEM [11]. Thus, continuity in velocity field solution is imposed. As another

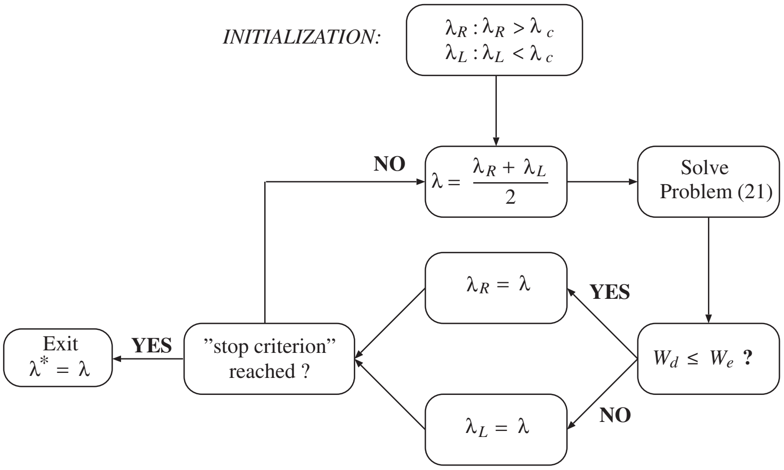

Figure 1. Optimal collapse load search algorithm.

consequence of this field approximation, subspace S only fulfills condition (13) and condition (14) is no longer valid. Regarding the approximation of the plastic strain rate field, local functions are considered for each finite element, without any relation with the adjacent elements.

In order to solve the mathematical programming problem (12), the following strategy is adopted:

- for a given load multiplier, λ, an optimal continuous kinematic field which minimizes the difference between dissipated and external work rate, J, is searched

$$\begin{aligned} \text{Min} \quad & J \\ \text{s.t.} \quad & \dot{\varepsilon} = B\dot{u} \\ & \dot{\varepsilon} \in \mathscr{C}_c \end{aligned} \tag{21}$$

  Since velocity and strain rate fields are independently approximated, the relationship between these two fields is established as a constraint in problem (21);
- following the kinematical theorem, if, for the optimal solution of (21), J value is non-positive, λ will unavoidably be an upper bound of the collapse load parameter ($\lambda \geqslant \lambda_c$). Otherwise, no conclusions can be drawn.

Therefore, the search for the best collapse load multiplier can be achieved by a simple iterative algorithm, as shown in Figure 1. The authors have improved the efficiency of the described algorithm with a few small adjustments. In fact, when the size of the search interval for the collapse load multiplier is smaller than a given threshold, the search for λ^* is carried out using algorithm 2 (Figure 2).

3.1. Mathematical programming problem

This section presents the method to solve the minimization problem (21). First, the augmented Lagrangian method [12] is applied to (21), thus producing the following velocity field minimization

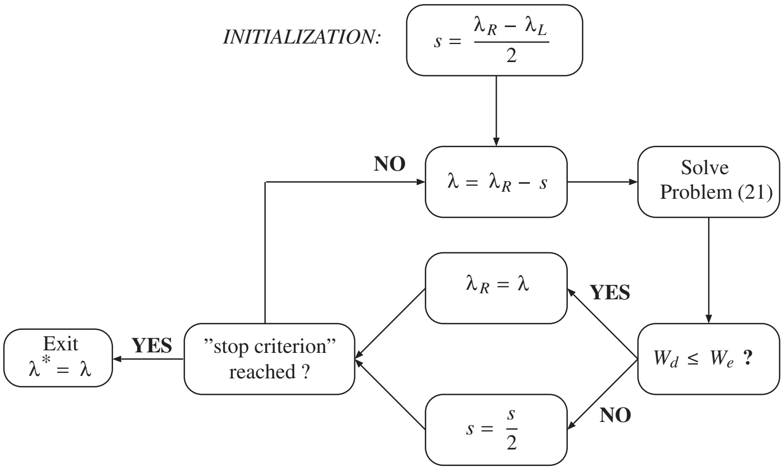

Figure 2. Optimal collapse load search algorithm 2.

problem:

$$\begin{aligned}\underset{\dot{\varepsilon}\in\mathscr{C}_c}{\text{Min}}\ \mathscr{L}(\dot{u},\dot{\varepsilon},\mu) &= \int_\Omega \mathscr{D}(\dot{\varepsilon})\,\mathrm{d}\Omega - \lambda\left(\int_\Omega b^{\mathrm{T}}\dot{u}\,\mathrm{d}\Omega + \int_{\Gamma_\sigma} t^{\mathrm{T}}\dot{u}\,\mathrm{d}\Gamma\right)\\ &\quad + \int_\Omega \mu:(B\dot{u}-\dot{\varepsilon})\,\mathrm{d}\Omega + \frac{r}{2}\int_\Omega \|B\dot{u}-\dot{\varepsilon}\|^2\,\mathrm{d}\Omega \qquad (22)\end{aligned}$$

where the μ vector collects the Lagrange multipliers and r denotes the penalty parameter, a positive scalar. In Equation (22), the first two terms are the J functional, where the discontinuity velocity term in the dissipated energy rate expression is cancelled out, since it is discarded by the finite element formulation. The last two terms introduce the compatibility constraint (8), present in problem (21), in the objective function.

Now, taking into consideration the finite element discretization of the domain and the field approximations (19)–(20), the augmented Lagrangian definition is re-written in the following expanded way:

$$\begin{aligned}\mathscr{L}(d,e,\mu) &= \sum_{i=1}^{n_E}\int_{\Omega_i}\mathscr{D}(E_i e_i)\,\mathrm{d}\Omega - \lambda\sum_{i=1}^{n_E}\left(\int_{\Omega_i} b^{\mathrm{T}}N_i\,\mathrm{d}\Omega + \int_{\Gamma_{\sigma i}} t^{\mathrm{T}}N_i\,\mathrm{d}\Gamma\right)d_i\\ &\quad + \sum_{i=1}^{n_E}\int_{\Omega_i}\mu_i^{\mathrm{T}}A_0(BN_i)\,\mathrm{d}\Omega d_i - \sum_{i=1}^{n_E}\int_{\Omega_i}\mu_i^{\mathrm{T}}A_0 E_i e_i\,\mathrm{d}\Omega\\ &\quad + \frac{r}{2}\sum_{i=1}^{n_E} d_i^{\mathrm{T}}\int_{\Omega_i}(BN_i)^{\mathrm{T}}A_0(BN_i)\,\mathrm{d}\Omega d_i - r\sum_{i=1}^{n_E} d_i^{\mathrm{T}}\int_{\Omega_i}(BN_i)^{\mathrm{T}}A_0(E_i e_i)\,\mathrm{d}\Omega\\ &\quad + \frac{r}{2}\sum_{i=1}^{n_E}\int_{\Omega_i}(E_i e_i)^{\mathrm{T}}A_0(E_i e_i)\,\mathrm{d}\Omega \qquad (23)\end{aligned}$$

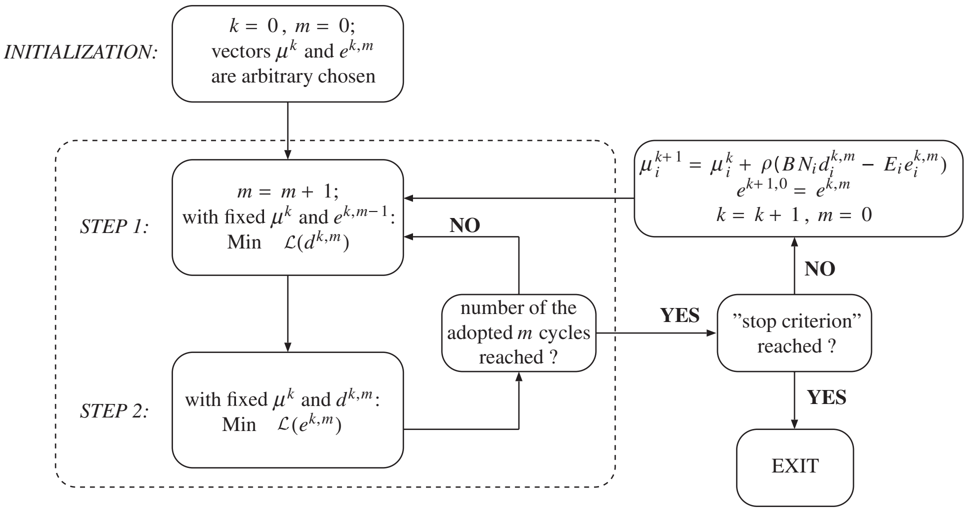

Figure 3. Uzawa's algorithm.

where the differential operator, B, the Lagrange multipliers vector, μ, and the A_0 matrix, assume the form:

$$B = \begin{bmatrix} \frac{\partial}{\partial_x} & \cdot & \cdot \\ \cdot & \frac{\partial}{\partial_y} & \cdot \\ \cdot & \cdot & \frac{\partial}{\partial_z} \\ \frac{\partial}{\partial_y} & \frac{\partial}{\partial_x} & \cdot \\ \cdot & \frac{\partial}{\partial_z} & \frac{\partial}{\partial_y} \\ \frac{\partial}{\partial_z} & \cdot & \frac{\partial}{\partial_x} \end{bmatrix}, \quad \mu_i = \begin{Bmatrix} \mu_x \\ \mu_y \\ \mu_z \\ 2\mu_{xy} \\ 2\mu_{yz} \\ 2\mu_{xz} \end{Bmatrix}_i, \quad A_0 = \begin{bmatrix} 1 & \cdot & \cdot & \cdot & \cdot & \cdot \\ \cdot & 1 & \cdot & \cdot & \cdot & \cdot \\ \cdot & \cdot & 1 & \cdot & \cdot & \cdot \\ \cdot & \cdot & \cdot & \frac{1}{2} & \cdot & \cdot \\ \cdot & \cdot & \cdot & \cdot & \frac{1}{2} & \cdot \\ \cdot & \cdot & \cdot & \cdot & \cdot & \frac{1}{2} \end{bmatrix}$$

To perform the minimization of the Langrangian (23), Uzawa's iterative saddle-point search algorithm can be used [13]. Figure 3 summarizes Uzawa's algorithm.

This algorithm displays quite a robust convergence, which is ensured whenever the number of inner iterations, m, is higher or equal to 1 ($m = 3$ was adopted) and the value of ρ belongs to the $[0, 2r]$ interval ($\rho = r$ was adopted). A fully detailed explanation of Uzawa's method and its convergence properties can be found in Reference [13].

Two independent minimizations must be carried out to perform Uzawa's algorithm. The first occurs during *STEP* 1, with respect to the nodal displacements and affects all the elements simultaneously. This minimization is straightforward. For variable d, the Lagrangian (23) is an unconstrained quadratic function. Thus, the minimizer is obtained by

$$\begin{aligned}\frac{\partial \mathscr{L}(d,e,\mu)}{\partial d} &= -\lambda \sum_{i=1}^{n_E}\left(\int_{\Omega_i} b^{\mathrm{T}} N_i \,\mathrm{d}\Omega + \int_{\Gamma_{\sigma i}} t^{\mathrm{T}} N_i \,\mathrm{d}\Gamma\right)\\ &\quad + \sum_{i=1}^{n_E}\int_{\Omega_i} \mu_i^{\mathrm{T}} A_0 (BN_i)\,\mathrm{d}\Omega + r\sum_{i=1}^{n_E}\int_{\Omega_i}(BN_i)^{\mathrm{T}} A_0 (BN_i)\,\mathrm{d}\Omega d_i\\ &\quad - r\sum_{i=1}^{n_E}\int_{\Omega_i}(BN_i)^{\mathrm{T}} A_0(E_i e_i)\,\mathrm{d}\Omega = 0 \end{aligned} \tag{24}$$

The result is a linear system of equations, which must be solved for each iteration. It can be expressed in the following matrix form:

$$[A]\{d\}^{k,m} = \lambda\{F\} - \{\Lambda\}^k + \{L\}^{k,m-1} \tag{25}$$

where,

$$[A] = r\sum_{i=1}^{n_E}\int_{\Omega_i}(BN_i)^{\mathrm{T}} A_0 (BN_i)\,\mathrm{d}\Omega \tag{26a}$$

$$\{F\} = \sum_{i=1}^{n_E}\left(\int_{\Omega_i} b^{\mathrm{T}} N_i\,\mathrm{d}\Omega + \int_{\Gamma_{\sigma i}} t^{\mathrm{T}} N_i\,\mathrm{d}\Gamma\right) \tag{26b}$$

$$\{\Lambda\}^k = \sum_{i=1}^{n_E}\int_{\Omega_i}(BN_i)^{\mathrm{T}} A_0(\mu_i)^k\,\mathrm{d}\Omega \tag{26c}$$

$$\{L\}^{k,m-1} = r\sum_{i=1}^{n_E}\int_{\Omega_i}(BN_i)^{\mathrm{T}} A_0(E_i e_i)^{k,m-1}\,\mathrm{d}\Omega \tag{26d}$$

Of note is the fact that the computational procedures of all the terms present in the governing system are, in all aspects, similar to the ones adopted for the FEM.

The second minimization takes place during *STEP* 2 of Uzawa's algorithm. In this stage, due to the definitions of the functions of plastic energy dissipation, $\mathscr{D}$ (summarized in Table I), the non-linearity of the problem emerges, which increases its complexity. However, the difficulties that arise from the minimization problem are confined to each finite element, by the adopted plastic strain approximation (20). In fact, it will be shown that this minimization can be solved individually, element by element.

3.2. Local minimization

By assuming variables d and μ as fixed throughout the local minimization process for variable e in every (k,m) iteration, the objective function (23) can be simplified for each finite element:

$$\begin{aligned}\mathscr{L}_i^*(e_i) &= \int_{\Omega_i}\mathscr{D}(E_i e_i)\,\mathrm{d}\Omega - \int_{\Omega_i}\mu_i^{\mathrm{T}} A_0 E_i e_i\,\mathrm{d}\Omega\\ &\quad - r\int_{\Omega_i}(BN_i d_i)^{\mathrm{T}} A_0(E_i e_i)\,\mathrm{d}\Omega + \frac{r}{2}\int_{\Omega_i}(E_i e_i)^{\mathrm{T}} A_0(E_i e_i)\,\mathrm{d}\Omega\end{aligned} \tag{27}$$

where, for notational simplicity, the k,m iteration superscripts were dropped out.

Let us now assume that the strain approximation functions matrix, E_i, is the identity matrix. This assumption has important consequences: (i) the strain rate field is constant for each element of the domain; (ii) e vector components gain a direct physical meaning as they represent the strain rate tensor components; (iii) the integrations in the above expression can be eliminated without affecting the optimality point

$$\mathscr{L}_i^*(e_i) = \mathscr{D}(e_i) - s^{\mathrm{T}} A_0\, e_i + \frac{r}{2} e_i^{\mathrm{T}} A_0 e_i \tag{28}$$

where

$$s_i = \{s_x, s_y, s_z, 2s_{xy}, 2s_{yz}, 2s_{zx}\}_i^{\mathrm{T}} = \mu_i + r B N_i d_i \tag{29}$$

(iv) to ensure final solution compatibility, the velocity approximation functions will be linear; therefore, 3-node triangle and 4-node tetrahedral isoparametric elements are used for 2D plane strain and 3D solid problems, respectively.

Mention must be made of the fact that at this stage of development it is not yet possible to extend the implementation of the model to higher order elements (i.e. elements with non-constant strain rate approximations), if a strict upper bound policy is required. The first obstacle is to impose the normality flow rule restriction to all the element domain ($\dot{\varepsilon} \in \mathscr{C}_c$). For linear strain elements, as shown in the work of Makrodimopoulos and Martin [14], this difficulty can, however, be overcome by imposing the normality rule on the element vertices. The second obstacle results from the fact that the mathematical complexity of the optimization subproblem (27) increases. In this case, the approach presented here to solve this minimization is no longer suitable, a procedure with proven efficiency has not been found so far.

A final step can be made to simplify the local minimization problem. According to Le Tallec [15], a new equivalent minimization problem, formulated in the principal strain space, can be derived and expressed as follows:

$$\operatorname*{Min}_{\tilde{e}_i \in \mathscr{C}} \mathscr{L}_i^*(\tilde{e}_i) = \mathscr{D}(\tilde{e}_i) - \tilde{s}_i^{\mathrm{T}} \tilde{e}_i + \frac{r}{2} \tilde{e}_i^{\mathrm{T}} \tilde{e}_i \tag{30}$$

where vector, $\tilde{e}_i = \{e_{\mathrm{I}}, e_{\mathrm{II}}, e_{\mathrm{III}}\}_i^{\mathrm{T}}$, collects the principal components of the domain strain rate tensor approximation, and vector $\tilde{s}_i$ gathers the S_i matrix eigenvalues, which are sorted in decreasing order ($s_{\mathrm{I}} \geqslant s_{\mathrm{II}} \geqslant s_{\mathrm{III}}$). The matrix S_i is defined by

$$S_i = \begin{bmatrix} s_x & s_{xy} & s_{zx} \\ s_{xy} & s_y & s_{yz} \\ s_{zx} & s_{yz} & s_z \end{bmatrix}_i \tag{31}$$

Of note is the fact that the first and last terms from the objective function (30) present an isotropic behaviour. On the contrary, for the middle term, each strain rate component is affected differently by the coefficients of $\tilde{s}_i$ vector. Therefore, it is possible to conclude, by taking into account the order adopted for these coefficients, that the optimal solution shares necessarily the same characteristic

$$e_{\mathrm{I}} \geqslant e_{\mathrm{II}} \geqslant e_{\mathrm{III}} \tag{32}$$

Another relevant property, stated in [15], is the following matrix orthogonal decomposition relationship:

$$\begin{bmatrix} e_x & e_{xy} & e_{zx} \\ e_{xy} & e_y & e_{yz} \\ e_{zx} & e_{yz} & e_z \end{bmatrix}_i = Y_i \begin{bmatrix} e_{\mathrm{I}} & \cdot & \cdot \\ \cdot & e_{\mathrm{II}} & \cdot \\ \cdot & \cdot & e_{\mathrm{III}} \end{bmatrix}_i Y_i^{\mathrm{T}} \tag{33}$$

Here, matrix Y_i collects, column-wise, the normalized eigenvectors of S_i matrix sorted in the same way as the eigenvalues.

The different procedures adopted to solve the minimization problem (30) are explained in detail in the Appendix, for the different yielding criteria.

3.3. Locking phenomenon

Tresca and von Mises criteria impose that plastic flow should occur under volumetric incompressibility conditions, by enforcing $\mathrm{tr}(\dot{\varepsilon})=0$ in Equation (7). Therefore, the locking phenomenon can emerge. This is a well-known numerical problem of finite elements displacement formulations, associated with incompressive kinematical behaviour, in which the solution becomes very inaccurate as a result of excessive stiffness of the model.

For Mohr–Coulomb and Drucker–Prager criteria, the admissible plastic strain domain ($\mathscr{C}_c$) is defined by a less or equal condition constraint which is less restrictive than the equality constraint, imposed by the isochoric materials. However, the inequality condition is restricted to plastic strains due to stress states located on the vertex of the yield surface. Thus, if the collapse problem under study is governed by a compressive failure behaviour, the equality condition is always activated and may affect the numerical results with a behaviour analogous to the volumetric locking, as shown in [16] for plane strain problems. Nevertheless, the authors avow from their experience that they never detected cases in which the results were manifestly affected by locking effects when using Mohr–Coulomb or Drucker–Prager materials.

In an attempt to overcome the locking problem, special geometric arrangements are used. In the case of 3-node triangle meshes, a very efficient distribution is proposed in Reference [17]: each set of four elements must form a quadrilateral with the central node in the intersection of the diagonals.

A similar procedure is adopted for 3D meshes: each assembly of 24 tetrahedrons must form a hexahedron with nodes positioned on every vertex; each face contains a middle node located in the intersection of the diagonals; finally, a central node is placed on the intersection of the diagonals of vertices. However, of note is the fact that this 3D combination of elements does not guarantee the elimination of the locking problem. To the best of our knowledge, no successful arrangement has so far proven suitable for this type of elements.

4. ILLUSTRATIVE RESULTS

In order to illustrate the performance and versatility of the proposed method, different classes of examples were studied. Whenever possible, the results are compared either with analytical solutions or with the outcome of other numerical formulations. All the results reported in this paper were

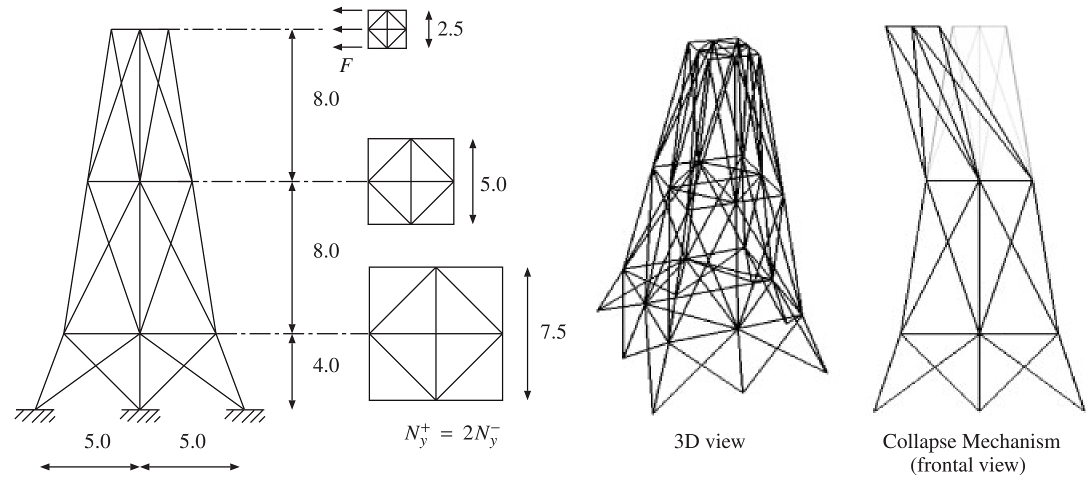

Figure 4. Strut-and-tie tower structure.

computed in a PC machine equipped with a Pentium IV 2.4 GHz CPU and a 1.0 GB RAM. The quadrilateral and hexahedral base meshes were generated using TrueGrid [18] software.

4.1. Strut-and-tie 3D structure

In this example, the plastic load of collapse of a strut-and-tie tower structure is computed. The tower, represented in Figure 4, consists of 114 bars and is subject to three concentrated loads at the top level. The yielding tension capacity, N_y^+, is the same for all bars and is the double of the value of the yielding compression capacity ($N_y^+ = 2N_y^-$).

The practical interest of this type of problems is limited, given that the bearing capacity of such structures is constantly dictated by instability phenomenon. Nevertheless, the 2-node bar element was implemented by taking into consideration its utility when conjugated with 2D and 3D elements.

This simple example was chosen not only to fully demonstrate the versatility of the proposed method, but also because, in this particular case, the finite element velocity approximation encloses all the kinematic admissible fields, i.e. condition (14) is verified. Thus, the exact collapse load is likely to be reached. As predicted, the exact collapse load, $F \simeq 0.97742 N_y^+$, was reached in 0.45 s. Figure 4 shows the attained collapse mechanism.

4.2. Prandtl's punch problem

As a plane strain example, we study the classical Prandtl's punch problem, which is represented in Figure 5. The strong discontinuity at the footing edge makes this problem numerically demanding. It places a challenge to the present method, which does not contemplate discontinuities in the velocity field.

First, the analysis of Tresca material was performed for two cases: (a) a rigid rough footing and (b) a perfectly flexible footing. The footing deformability does not alter the upper bound approximation of the collapse load value, which is in accordance with Prandtl's analytical solution

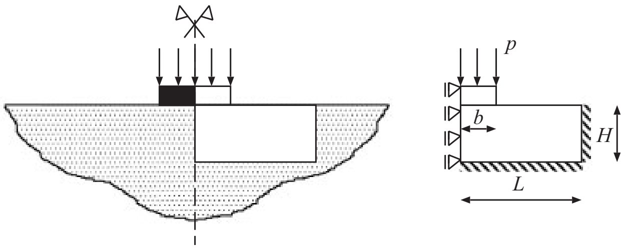

Figure 5. Prandtl's punch problem: model geometry.

Table II. Prandtl's punch problem for Tresca material: comparison of solutions by different methods.

Authors and methods	Scaled collapse load	Time (s)
Analytical [19]	$2+\pi \simeq 5.142$	—
Present work (b)	5.170	52
Tin-Loi and Ngo [20]	5.173	—
Capsoni [21]	5.191	—
Sloan and Kleeman [1]	5.210	—
Capsoni and Corradi [22]	5.240	—
Present work (a)	5.264	57

[19]. A mesh of 4784 3-node elements was used to discretize the domain, defined for $H=2b$ and $L=4b$. In an attempt to overcome the singularity caused by the footing extremity, the mesh density was increased below that region. Table II presents, using the dimensionless parameter $2p/\sigma_0$, the collapse loads obtained and the respective CPU times. The results proved to be competitive with other methods and showed a very good accuracy when compared with the analytical solution. As expected, it is in case (a), in which the footing rigidity imposes a stronger singularity, that the larger discrepancy with the exact solution is observed. Even so, the error in this case did not exceed 2.4%. Better results can be attained by increasing the number of finite elements, since these analyses only required about 5% of the available memory and a reduced CPU time. In fact, a more refined mesh using 28 212{38 572} elements was tested for the rigid footing scenario and a value of 5.204{5.198} was attained for the upper bound estimated value, which corresponds to a 1.21%{1.10%} error value. The CPU time in this case was 405{684} s.

Figure 6 illustrates the distribution of the plastic dissipation energy rate of collapse (normalized to the maximum value) and the respective collapse mechanisms. These dissipation patterns clearly indicate that the two cases under study form different punch mechanisms. In case (a), the mechanism is similar to the one proposed by Prandtl [19], with a single large rigid block under the footing. Case (b) presents a more similar mechanism with the one proposed by Hill [23]. Another difference between the two solutions is the fact that in case (a) the plastic dissipation is more concentrated on narrower regions, approaching the form of well-defined slip lines.

The punch collapse load problem is also analysed using Mohr–Coulomb material with different shearing resistance angles (ϕ), considering only the perfectly flexible footing case. The results are juxtaposed with the analytical curve [19] in the graph of Figure 7. Once more, the results match the exact solution perfectly. The error never exceeds 1.87%. The highest CPU time of

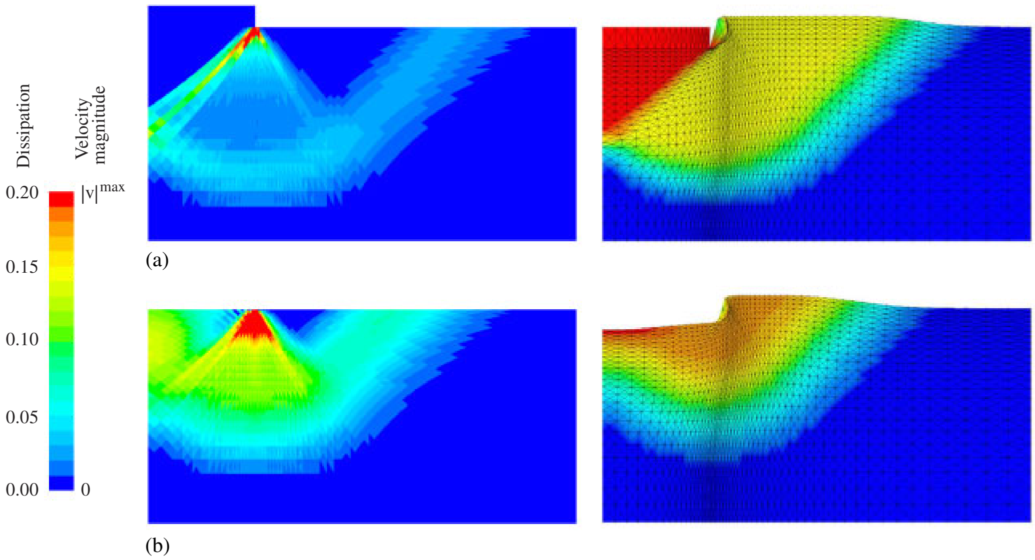

Figure 6. Prandtl's punch problem: plastic dissipation energy rate and collapse mechanism: (a) rigid footing and (b) flexible footing.

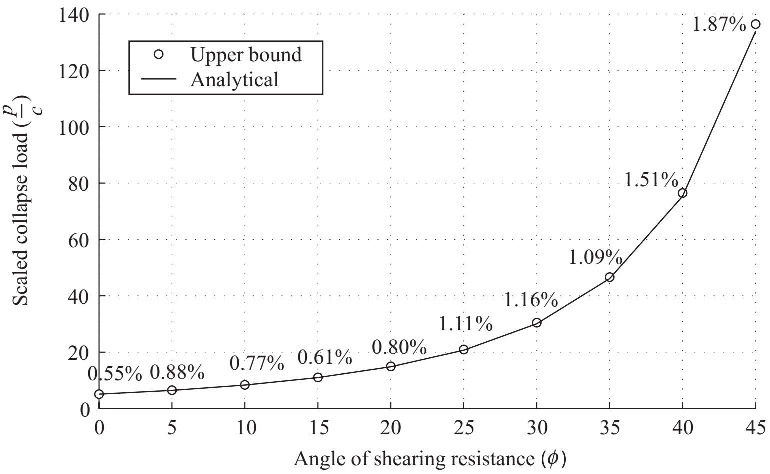

Figure 7. Punch problem: scaled collapse load and relative error for Mohr–Coulomb material.

487 s and available memory use of 22% occurred during the computations for a ϕ value of 35° and 45°, respectively. The increase in ϕ value expands the region of the collapse mechanisms. Therefore, the analysis domain had to be amplified for higher values of ϕ, which required the use of more finite elements to maintain the level of accuracy. This procedure justifies the increasing use of computational resources when compared with the ones used during the analysis with Tresca

DOI: 10.1002/nme

Table III. Influence of h-refinement on the upper bound solution for $\phi = 35°$.

h/b	Total number of elements	p/c	Error (%)	Time (s)
0.500	2016	49.71	7.78	20
0.250	8064	47.96	3.99	105
0.167	18 144	47.42	2.81	344
0.125	32 256	47.11	2.14	1016
0.100	50 400	46.92	1.73	1140
0.083	72 576	46.80	1.47	1888
0.071	98 784	46.71	1.27	2921

material. Of note is, for instance, the fact that for $\phi = 45°$, the region of $H = 5b$ and $L = 15b$ was discretized and 31 752 finite elements were used.

In order to illustrate the influence of the h-refinement on the obtained solutions and the limitations of the proposed model in obtaining the best approximation of the upper bound load, a set of calculations for the same shearing resistance angle were performed. In these calculations, all the meshes were regular, in the sense that the size of the elements was the same in all the domains. For ϕ, a value of 35° was adopted, since this was the most time-consumming task of all the computations for the results reported in Figure 7. Table III shows the values of the upper bound calculated with the regular meshes. The level of mesh refinement is defined by parameter h, which represents the length of the elements in the quadrilateral base mesh. The h-refinement was performed within the maximum extent of the available computer capacities, leading to a 92% memory use for the most refined mesh.

The analysis of the Table III makes it possible to conclude that:

- Although the resources employed in the regular mesh computations are a few times greater than those used in the previous calculations, the results are worse. This can be justified by the fact that the singularity of the problem cannot be as easily overcome with a regular mesh as with a variable density mesh.
- Uniform meshes are not suitable for this type of problems.

These points show the need for developing in the near future an adaptive mesh approach. Despite the works already published as regards mesh adaptivity in limit analysis field ([24–26], etc.) the authors consider that it is essential to adapt/develop an approach that takes into account the particularities of the present formulation.

Figure 8 shows the collapse load mechanism and the plastic energy dissipation rate obtained for this case. The results shown for the collapse mechanism regard the coarsest studied mesh due to limitations in graph representation. As for the plastic energy dissipation rate representation, the results for both the finest and the coarsest mesh are represented. These results demonstrate an obvious improvement in the dissipation pattern with mesh refinement. It should be noted that the minimization programme leads to an optimal velocity field without requiring, from the user, any guidelines for its configuration.

4.3. Perforated square plate

For the plane stress case example, a square plate perforated with a concentric circular hole of von Mises material, subject to a uniform biaxial traction, is considered, as shown in Figure 9. This

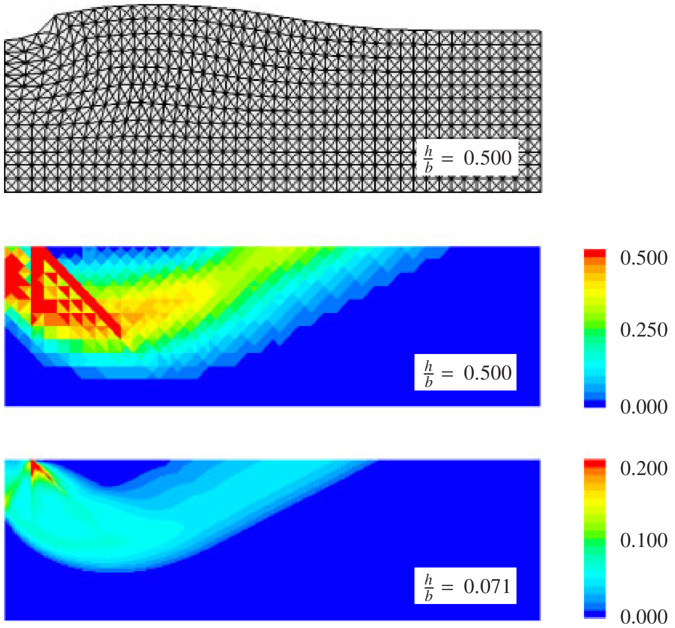

Figure 8. Collapse mechanism configuration and plastic energy dissipation rate for $\phi = 35°$.

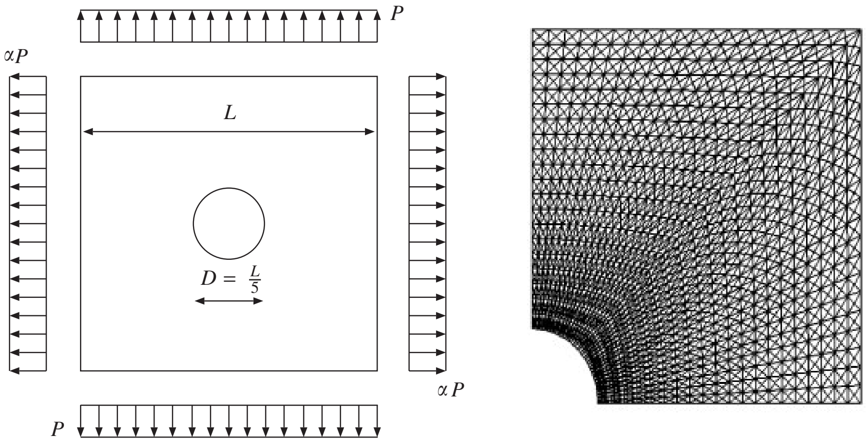

(a) (b)

Figure 9. Perforated square plate: (a) geometry and loading (b) finite element mesh.

problem is a benchmark test, which has been studied by several authors. For symmetry reasons, only a quarter of the plate was analysed. Figure 9 shows the domain discretization using 3200 finite elements. Three different loading cases, defined by the load ratio parameter, α, equal to 1, $\frac{1}{2}$ and 0, respectively, were analysed. These analyses required an average CPU time of 73 s.

Table IV. Perforated square plate: comparison of solutions by different methods.

Approach	Authors	Loading cases $\alpha=1$	$\alpha=1/2$	$\alpha=0$
Analytical	Gaydon and McCrum [27]	—	—	0.800
Incremental	INTES [28]	0.904	—	—
Static	Groß-Weege [29]	0.882	0.891	0.782
	Tin-Loi and Ngo [20]	0.845	0.912	0.803
	Liu *et al.* [30]	0.903	0.915	0.795
Kinematic	Present work	0.899	0.915	0.807

The results for the scaled collapse loads, $P/\sqrt{3}k$, are summarized in Table IV together with those obtained by other authors using different methods. The present results are found to be in good agreement with those of other methods. When compared with the analytical solution for the $\alpha=0$ case, the only one available to our knowledge, a difference of merely 0.875% is observed. Reference must be made to the fact that the lower bound collapse load estimate by Liu *et al.* [30], for the $\alpha=1$ load case, surpasses the upper bound value of the present work. This fact can be justified since, in the Liu *et al.* method, the static limit analysis theorem is not strictly imposed. A similar phenomenon can be observed in Tin-Loi and Ngo [20], in which the lower bound estimate exceeds the exact value for the $\alpha=0$ load case. Figure 10 presents the patterns of plastic energy dissipation and the configuration of collapse mechanisms for the three load cases studied.

4.4. *Defective pipeline*

The 3D defective pipeline collapse load problem represented in Figure 11 has been studied by Liu *et al.* [30] using both an incremental method and a limit analysis method based on a boundary element formulation of the static theorem approach. A von Mises material is adopted, which is characterized by a shear yield stress of $k=200/\sqrt{3}$ MPa. Two distinct load cases are considered: (i) an internal pressure, p, associated with a proportional axial stress, $p_N=\pi R_i^2 p$; (ii) a bending moment M, applied through a p_M stress distribution.

This example was chosen because it contains two numerical difficulties associated with 3D problems for the present method. On the one hand, the local minimization of von Mises criterion requires an iterative procedure, a relevant time-consumming factor. On the other hand, von Mises' volumetric incompressibility may cause locking problems.

By taking into account the symmetry of the problem, the hexahedral base mesh represented in Figure 12 was adopted. The results, reported in Table V, show a satisfactory compliance with the values of Reference [30]. However, of note is the fact that the level of accuracy of the results is lower when compared with the results of the prior 2D examples. The previously mentioned locking effects and the lower mesh refinement degree are probably the cause for this discrepancy. Figure 13 depicts the collapse mechanisms for each load case studied.

4.5. *Circular footing punch problem*

The next example analyses the load p bearing capacity of a smooth, rigid circular footing in a semi-infinite media of Mohr–Coulomb material. The results obtained for several shearing resistance

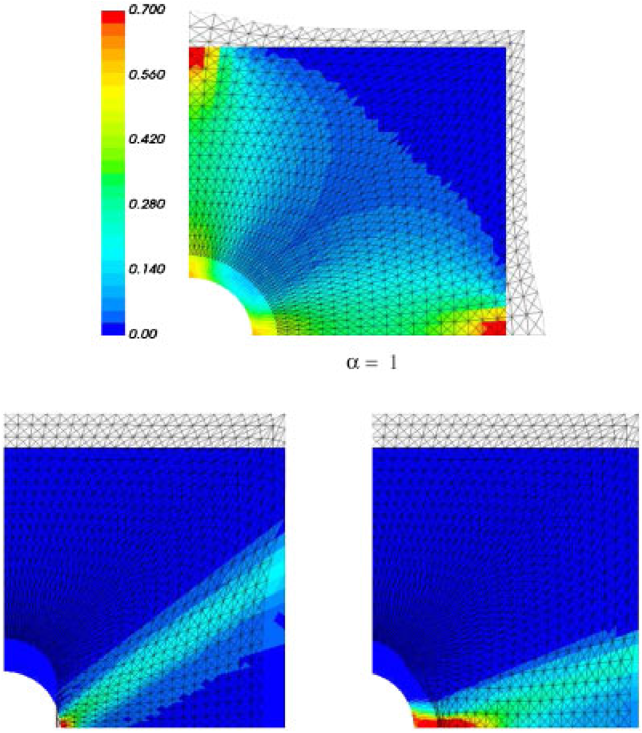

$\alpha = 1$

$\alpha = 0$ $\alpha = \frac{1}{2}$

Figure 10. Plastic dissipation pattern and collapse mechanisms configurations.

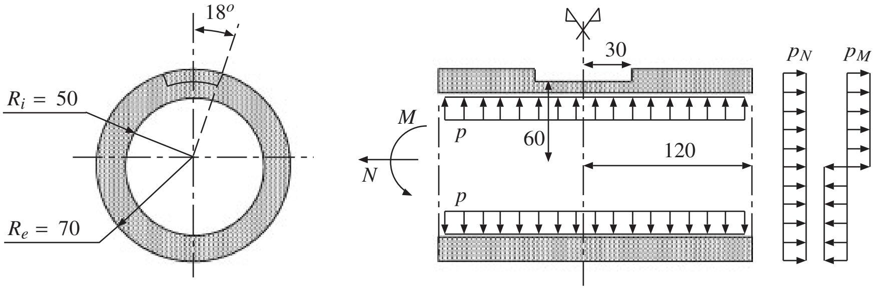

Figure 11. Defective pipeline.

angles (ϕ) are presented in Table VI and compared with the exact solution derived by Cox *et al.* [31]. The same table also shows the values computed by an accurate lower bound method proposed by Lyamin and Sloan [6].

By taking into consideration the axisymmetry of the problem, only a 5° slice was studied, using meshes of a fixed number of 45 541 tetrahedral finite elements. This number of elements required 36% of the available memory. The length and depth of the meshes were adjusted according to

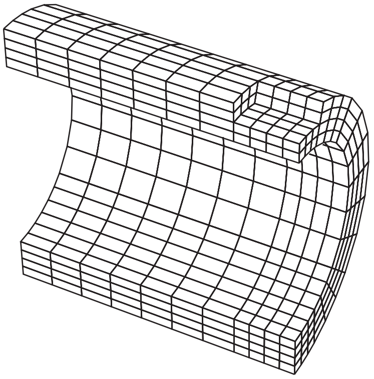

Figure 12. Defective pipeline: hexahedral base mesh.

Table V. Defective pipeline: comparison of solutions by different methods.

		Case a		Case b	
Approach	Authors	Collapse pressure (MPa)	Time (s)	Collapse moment (kN m)	Time (s)
Kinematic	Present work	67.13	697	56.02	611
Incremental	Liu *et al.* [30]	64.05	—	55.27	—
Static	Liu *et al.* [30]	63.42	—	54.96	—

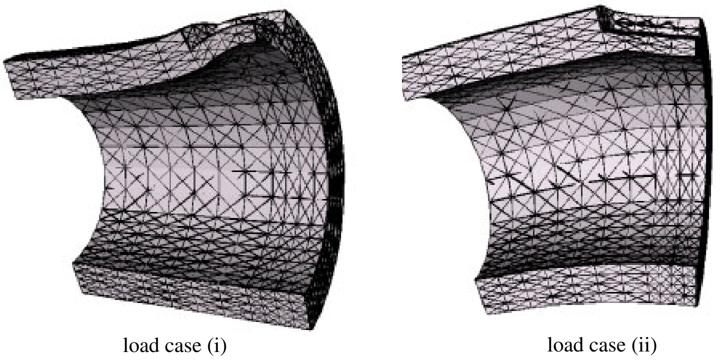

load case (i) load case (ii)

Figure 13. Defective pipeline: configurations of the collapse mechanisms.

angle ϕ. As in the Prandtl punch problem, the singularities at the edge of the footing pose a numerical constraint to the present method. In order to overcome this problem, the mesh elements were refined in this region.

For the friction angle of $\phi = 40°$, the colapse load obtained showed that the originally adopted mesh was not able to produce satisfactory results. Therefore, a new mesh of 52 981 elements was

DOI: 10.1002/nme

Table VI. Circular footing punch problem: comparison of solutions by different methods.

	Upper bound (present work)			Analytical [31]	Lower bound [6]	
ϕ (deg.)	p/c	Error (%)	Time (s)	p/c	p/c	Error (%)
0	5.80	+1.93	1102	5.69	5.54	−2.64
5	7.60	+2.15	1063	7.44	7.2	−3.23
10	10.26	+2.81	1085	9.98	9.61	−3.71
15	14.34	+3.17	1081	13.9	13.3	−4.32
20	20.80	+3.48	1266	20.1	19.06	−5.17
30	51.9	+5.27	1696	49.3	—	—
40	180.6	+10.12	1601	164	—	—
	174.4*	+6.34*	2176*			

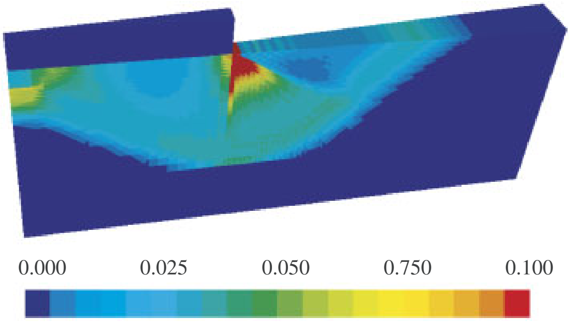

Figure 14. Scaled plastic dissipation energy rate for $\phi = 15°$.

analysed. The collapse load obtained for this second mesh is presented in Table VI marked with a star (*). The upper bounds predicted by the present method can be considered very accurate for this type of problems. The computational costs are significant, but acceptable for this level of accuracy in this kind of problems. Figure 14 shows the plastic dissipation energy rate for $\phi = 15°$, scaled to the maximum obtained value.

4.6. *Conic excavation stability*

Lastly, to conclude the example section, the stability of a conical excavation subject to its self-weight, γ, is analysed. The depth and the diameter at the base of the excavation correspond to 5 and 2 m, respectively. In order to simulate the soil behaviour, a cohesive-frictional material was assumed, with a cohesion of $c = 1$ kPa and a friction angle of $\phi = 20°$, using both Mohr–Coulomb and Ducker–Prager criteria.

The results obtained for a range of slope angles, β, are summarized in Table VII and compared with the solutions obtained with a discontinuous upper bound formulation [32]. Once more, the axisymmetry of the problem was taken into account: only a 15° slice was discretized with the proper symmetry boundary conditions. In all the meshes adopted during the analyses of the different slope angle excavations, a fixed number of 24 468 elements was used. This discretization results in a total of 181 456 problem unknowns, embodied by 17 324 and 164 132 degrees of freedom for the velocity and strain rate field, respectively. For this same problem, a total of 325 206

Table VII. Conic excavation stability: upper bound values and CPU time.

	Present method				Discontinuous formulation [32]			
	Mohr–Coulomb		Drucker–Prager		Mohr–Coulomb		Drucker–Prager	
β (deg.)	$\gamma H/c$	Time (s)	$\gamma H/c$	Time (s)	$\gamma H/c$	Time (s)	$\gamma H/c$	Time (s)
50	27.73	443	25.63	447	27.72	3120	25.75	532
60	22.27	483	20.79	485	22.34	2700	20.80	486
70	19.22	318	17.99	384	19.25	2580	18.06	443
80	17.71	539	16.50	431	17.55	2280	16.52	378

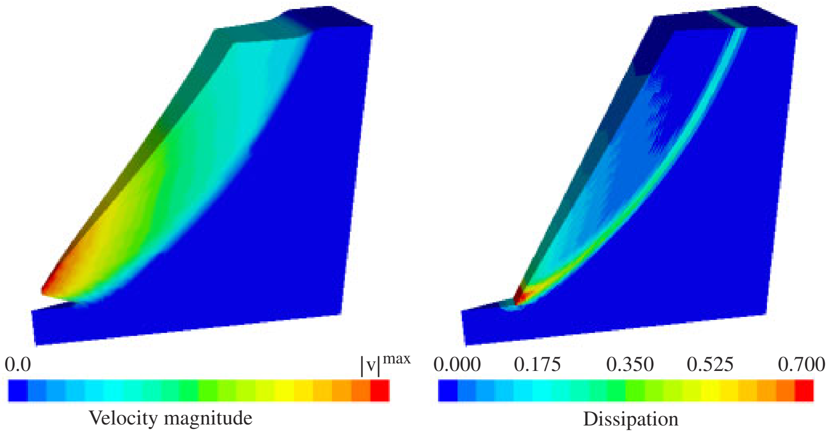

Figure 15. Collapse load mechanism and scaled plastic dissipation energy rate for $\beta = 60°$.

problem unknowns were required to obtain the solutions reported by Krabbenhøft *et al.* [32], used as reference. Mention must be made of the fact that the analysis in [32] was performed in an architecture about 1.4 × slower than the one used to compute the results for the current work.

The results reveal not only a good agreement with those of [32], but also with the upper and lower bound estimates produced by different formulations, also mentioned in the paper referred to above. Taken as a whole, the results show a better accuracy when compared with the upper bound reference values, and even for the worse result obtained the relative error never exceeds 0.9%. This fact supports the authors' opinion, expressed in Section 2.3, that the continuity assumption does not affect significantly the accuracy of the method and may represent a computational speed up. In fact, the authors consider that a discontinuous formulation would represent an advantage particularly if conjugated with a proper adaptive mesh approach.

Another important feature of the present model, corroborated by these results, is its aptitude to deal with non-smooth yielding criteria without affecting the convergence rate of the method and consequently the computational time.

Figure 15 shows the configuration of the collapse mechanism and the plastic energy dissipation rate for a slope angle excavation of 60°, using Mohr–Coulomb criterion.

DOI: 10.1002/nme

5. CLOSURE

This paper implemented a finite element formulation using mathematical non-linear programming for computing collapse loads estimates and the respective failure mechanisms, based on the kinematical upper bound theorem of limit analysis.

Implementation and computational aspects were discussed for Tresca, von Mises, Mohr–Coulomb and Drucker–Prager yielding criteria. To perform domain space discretization, 2-node bars, 3-node plane triangles and 4-node tetrahedral isoparametric elements were used. To avoid or to diminish the locking phenomenon, particular geometric arrangements of finite elements were used during mesh generation.

The efficiency, accuracy and robustness of the proposed method were demonstrated using some numerical examples. The latter also demonstrate the versatility of the method that can be applied to solve a wide range of collapse problems.

APPENDIX A: TRESCA MINIMIZATION CRITERION

A.1. 3D solid problems

As a starting point, the constraint of problem (30) is eliminated, by considering the definition of $\mathscr{C}_c$ (Table I) and the number of independent variables is reduced, using the following relationship:

$$e_{\mathrm{III}} = -e_{\mathrm{I}} - e_{\mathrm{II}} \tag{A1}$$

Introducing (A1) into the objective function, a $\mathbb{R}^2$ piecewise quadratic function is obtained

$$\begin{aligned}\mathscr{L}^*(e_{\mathrm{I}}, e_{\mathrm{II}}) = {} & \frac{\sigma_0}{2}(|e_{\mathrm{I}}| + |e_{\mathrm{II}}| + |e_{\mathrm{I}} + e_{\mathrm{II}}|) \\ & + r(e_{\mathrm{I}}^2 + e_{\mathrm{II}}^2 + e_{\mathrm{I}}e_{\mathrm{II}}) + (s_{\mathrm{III}} - s_{\mathrm{I}})e_{\mathrm{I}} + (s_{\mathrm{III}} - s_{\mathrm{II}})e_{\mathrm{II}}\end{aligned} \tag{A2}$$

By taking into account condition (32), only four regions should be considered: $e_{\mathrm{I}} = 0 \wedge e_{\mathrm{II}} = 0$, $e_{\mathrm{I}} > 0 \wedge e_{\mathrm{II}} = 0$, $e_{\mathrm{I}} > 0 \wedge e_{\mathrm{II}} > 0$ and $e_{\mathrm{I}} > 0 \wedge e_{\mathrm{II}} < 0$ the following points become thus feasible candidates for a minimizer:

$$\begin{aligned}
\tilde{e}^1 &= \{0, 0, e_{\mathrm{III}}\}^{\mathrm{T}} \\
\tilde{e}^2 &= \left\{-\frac{\sigma_0 - s_{\mathrm{I}} + s_{\mathrm{III}}}{2r}, 0, e_{\mathrm{III}}\right\}^{\mathrm{T}} \\
\tilde{e}^3 &= \left\{-\frac{\sigma_0 - 2s_{\mathrm{I}} + s_{\mathrm{II}} + s_{\mathrm{III}}}{3r}, -\frac{\sigma_0 - 2s_{\mathrm{II}} + s_{\mathrm{I}} + s_{\mathrm{III}}}{3r}, e_{\mathrm{III}}\right\}^{\mathrm{T}} \\
\tilde{e}^4 &= \left\{-\frac{2\sigma_0 - 2s_{\mathrm{I}} + s_{\mathrm{II}} + s_{\mathrm{III}}}{3r}, -\frac{-\sigma_0 - 2s_{\mathrm{II}} + s_{\mathrm{I}} + s_{\mathrm{III}}}{3r}, e_{\mathrm{III}}\right\}^{\mathrm{T}}
\end{aligned} \tag{A3}$$

The most basic and yet efficient procedure to attain the minimizer is to test all these points and select the best one.

A.2. 2D plane strain problems

In this case, an extra and obvious condition is naturally imposed

$$e_{\mathrm{III}}=0 \tag{A4}$$

and the feasible points are reduced to two

$$\begin{aligned}\tilde{e}^1&=\{0,\ 0\}^{\mathrm{T}}\\ \tilde{e}^2&=\left\{\frac{-\sigma_0+s_{\mathrm{I}}-s_{\mathrm{II}}}{2r},\ \frac{\sigma_0-s_{\mathrm{I}}+s_{\mathrm{II}}}{2r}\right\}^{\mathrm{T}}\end{aligned} \tag{A5}$$

APPENDIX B: VON MISES MINIMIZATION CRITERION

B.1. 3D solid problems

Similarly to the Tresca criterion, the constraint of the problem is eliminated and relationship (A1) is applicable. However, this time a non-linear objective function is obtained

$$\mathscr{L}^*(e_{\mathrm{I}},e_{\mathrm{II}})=2k\sqrt{e_{\mathrm{I}}^2+e_{\mathrm{II}}^2+e_{\mathrm{I}}e_{\mathrm{II}}}+r(e_{\mathrm{I}}^2+e_{\mathrm{II}}^2+e_{\mathrm{I}}e_{\mathrm{II}})+(s_{\mathrm{III}}-s_{\mathrm{I}})e_{\mathrm{I}}+(s_{\mathrm{III}}-s_{\mathrm{II}})e_{\mathrm{II}} \tag{B1}$$

To solve this unconstrained minimization problem, the Fletcher–Reeves algorithm [12] is used, as described below. This algorithm is adapted from the conjugated gradient method and is suitable for convex non-linear optimization. Each iteration step is obtained by

$$\{e_{\mathrm{I}},e_{\mathrm{II}}\}_{k+1}^{\mathrm{T}}=\{e_{\mathrm{I}},e_{\mathrm{II}}\}_k^{\mathrm{T}}+\alpha_k p_k,\quad \alpha_k\in\mathbb{R}^+ \tag{B2}$$

where α_k is the step length and p_k is the step direction

$$p_k=\{p_1,\ p_2\}_k^{\mathrm{T}}=-\nabla\mathscr{L}_k^*+\frac{\nabla\mathscr{L}_k^{*\mathrm{T}}\nabla\mathscr{L}_k^*}{\nabla\mathscr{L}_{k-1}^{*\mathrm{T}}\nabla\mathscr{L}_{k-1}^*}p_{k-1} \tag{B3}$$

The expression for the objective function gradient is given by

$$\nabla\mathscr{L}^*(e_{\mathrm{I}},e_{\mathrm{II}})=\left\{\begin{array}{c}\dfrac{k(2e_{\mathrm{I}}+e_{\mathrm{II}})}{\sqrt{e_{\mathrm{I}}^2+e_{\mathrm{II}}^2+e_{\mathrm{I}}e_{\mathrm{II}}}}+r(2e_{\mathrm{I}}+e_{\mathrm{II}})-s_{\mathrm{I}}+s_{\mathrm{III}}\\ \dfrac{k(2e_{\mathrm{II}}+e_{\mathrm{I}})}{\sqrt{e_{\mathrm{I}}^2+e_{\mathrm{II}}^2+e_{\mathrm{I}}e_{\mathrm{II}}}}+r(2e_{\mathrm{II}}+e_{\mathrm{I}})-s_{\mathrm{II}}+s_{\mathrm{III}}\end{array}\right\} \tag{B4}$$

The best step length for $k+1$ iteration can be accomplished by solving the following problem:

$$\mathrm{Min}\ \mathscr{L}_k^*(e_{\mathrm{I}}+\alpha p_1,e_{\mathrm{II}}+\alpha p_2) \tag{B5}$$

However, performing this exact minimization for every iteration is computationally very demanding. Instead, a good estimate is obtained by expanding this objective function in Taylor series (truncated in the quadratic term) and by solving the resulting minimization problem analytically, thus deriving the next explicit formula

$$\begin{aligned}\alpha = &-\left[\frac{k(2e_{\mathrm{I}}p_1 + 2e_{\mathrm{II}}p_2 + e_{\mathrm{I}}p_2 + e_{\mathrm{II}}p_1)}{\sqrt{e_{\mathrm{I}}^2 + e_{\mathrm{II}}^2 + e_{\mathrm{I}}e_{\mathrm{II}}}} + r(2e_{\mathrm{I}}p_1 + 2e_{\mathrm{II}}p_2 + e_{\mathrm{I}}p_2 + e_{\mathrm{II}}p_1)\right.\\ &\left. - s_{\mathrm{I}}p_1 - s_{\mathrm{II}}p_2 + s_{\mathrm{III}}(p_1 + p_2)\right] \Big/ \left[\frac{3k(e_{\mathrm{I}}p_2 - e_{\mathrm{II}}p_1)^2}{2(e_{\mathrm{I}}^2 + e_{\mathrm{I}}e_{\mathrm{II}} + e_{\mathrm{II}}^2)^{2/3}}\right.\\ &\left. + 2r(p_{\mathrm{I}}^2 + p_2^2 + p_1p_2)\right] \qquad \text{(B6)}\end{aligned}$$

For notational simplicity, the k iteration superscript was dropped out. To start the algorithm, the initial step direction is given by $\nabla\mathscr{L}_0^*$. A first reasonable guess of the solution is also needed. Prior simulations suggest as a good estimate the following point:

$$\begin{Bmatrix} e_{\mathrm{I}} \\ e_{\mathrm{II}} \end{Bmatrix}_0 = \begin{Bmatrix} \dfrac{2s_{\mathrm{I}} - s_{\mathrm{II}} - s_{\mathrm{III}}}{3(r+k)} \\ \dfrac{2s_{\mathrm{II}} - s_{\mathrm{I}} - s_{\mathrm{III}}}{3(r+k)} \end{Bmatrix} \qquad \text{(B7)}$$

B.2. 2D plane strain problems

For 2D plane strain problems, this criterion coincides with the Tresca criterion and, therefore, the same optimization procedure can be used, with $\sqrt{3}k = \sigma_0$.

APPENDIX C: MOHR–COULOMB MINIMIZATION CRITERION

C.1. 3D solid problems

A different strategy from the ones presented above is used to solve the Mohr–Coulomb criterion minimization. We now stand before a quadratic objective function, subject to piecewise linear inequality constraints.

Let us start by solving the problem regardless of constraints. In this case, the unconstrained solution, $\widetilde{e}_u$, is given by

$$\widetilde{e}_u = \{o_1, o_2, o_3\}^{\mathrm{T}} = \frac{1}{r}\left\{-\frac{c}{\tan(\phi)} + s_{\mathrm{I}}, -\frac{c}{\tan(\phi)} + s_{\mathrm{II}}, -\frac{c}{\tan(\phi)} + s_{\mathrm{III}}\right\}^{\mathrm{T}} \qquad \text{(C1)}$$

Subsequently, the previous solution is tested to check if it belongs to the feasible domain, $\widetilde{e}_u \in \mathscr{C}$. If so, the optimality point is reached. Otherwise, the solution consists in the closest point of the unconstrained optimal point, located on the feasible domain surface [33]

$$\mathrm{tr}(\dot{\varepsilon}) = (|\dot{\varepsilon}_{\mathrm{I}}| + |\dot{\varepsilon}_{\mathrm{II}}| + |\dot{\varepsilon}_{\mathrm{III}}|)\sin\phi \qquad \text{(C2)}$$

In fact, the coefficients affecting the quadratic terms of the objective function are the same $(r/2)$. Therefore, the equipotential of the function surfaces define spheres centred on the unconstrained optimal point. Given that the feasible domain is convex, the optimal point is necessarily the point of the feasible domain nearest to the centre. According to restriction (32), only the following four points are admissible candidates:

$$\widetilde{e}^1 = \{0, 0, 0\}^{\mathrm{T}} \tag{C3a}$$

$$\widetilde{e}^2 = \left\{ \begin{array}{c} -(1+\sin(\phi))\dfrac{(2H - s_{\mathrm{III}} - s_{\mathrm{I}})\sin(\phi) - s_{\mathrm{I}} + s_{\mathrm{III}}}{2r(\sin(\phi)^2+1)} \\ 0 \\ -\dfrac{(2H - s_{\mathrm{III}} - s_{\mathrm{I}})\sin(\phi)^2 + 2(s_{\mathrm{III}} - H)\sin(\phi) + s_{\mathrm{I}} - s_{\mathrm{III}}}{2r(\sin(\phi)^2+1)} \end{array} \right\} \tag{C3b}$$

$$\widetilde{e}^3 = \left\{ \begin{array}{l} o_1 - (1-\sin(\phi))\dfrac{(1-\sin(\phi))o_1 + (1-\sin(\phi))o_2 + (1+\sin(\phi))o_3}{2(1-\sin(\phi))^2 + (1+\sin(\phi))^2} \\ o_2 - (1-\sin(\phi))\dfrac{(1-\sin(\phi))o_1 + (1-\sin(\phi))o_2 + (1+\sin(\phi))o_3}{2(1-\sin(\phi))^2 + (1+\sin(\phi))^2} \\ o_3 - (1+\sin(\phi))\dfrac{(1-\sin(\phi))o_1 + (1-\sin(\phi))o_2 + (1+\sin(\phi))o_3}{2(1-\sin(\phi))^2 + (1+\sin(\phi))^2} \end{array} \right\} \tag{C3c}$$

$$\widetilde{e}^4 = \left\{ \begin{array}{l} o_1 - (1-\sin(\phi))\dfrac{(1-\sin(\phi))o_1 + (1+\sin(\phi))o_2 + (1+\sin(\phi))o_3}{(1-\sin(\phi))^2 + 2(1+\sin(\phi))^2} \\ o_2 - (1+\sin(\phi))\dfrac{(1-\sin(\phi))o_1 + (1+\sin(\phi))o_2 + (1+\sin(\phi))o_3}{(1-\sin(\phi))^2 + 2(1+\sin(\phi))^2} \\ o_3 - (1+\sin(\phi))\dfrac{(1-\sin(\phi))o_1 + (1+\sin(\phi))o_2 + (1+\sin(\phi))o_3}{(1-\sin(\phi))^2 + 2(1+\sin(\phi))^2} \end{array} \right\} \tag{C3d}$$

Choosing the minimizer involves the following steps: (i) confirming if the points comply with Equation (C2); (ii) selecting, from among all the points that satisfy the previous condition, the one that minimizes the objective function (30).

C.2. 2D plane strain problems

The same procedure can be applied to 2D plane strain problems. Taking into account condition (A4) the unconstrained solution, $\widetilde{e}_u$, is therefore given by

$$\widetilde{e}_u = \{o_1, o_2\}^{\mathrm{T}} = \frac{1}{r}\left\{ -\frac{c}{\tan(\phi)} + s_{\mathrm{I}}, -\frac{c}{\tan(\phi)} + s_{\mathrm{II}} \right\}^{\mathrm{T}} \tag{C4}$$

and the possible candidates located on the surface domain are reduced to two

$$\widetilde{e}^1 = \{0, 0\}^{\mathrm{T}} \tag{C5a}$$

$$\widetilde{e}^2 = \left\{ \begin{array}{l} o_1 - (1-\sin(\phi))\dfrac{(1-\sin(\phi))o_1 + (1+\sin(\phi))o_2}{(1-\sin(\phi))^2 + (1+\sin(\phi))^2} \\ o_2 - (1+\sin(\phi))\dfrac{(1-\sin(\phi))o_1 + (1+\sin(\phi))o_2}{(1-\sin(\phi))^2 + (1+\sin(\phi))^2} \end{array} \right\} \tag{C5b}$$

A more detailed discussion about this minimization can be found in Reference [33].

APPENDIX D: DRUCKER–PRAGER MINIMIZATION CRITERION

D.1. 3D solid problems

The local minimization for the Drucker–Prager criterion follows the same procedure adopted for the Mohr–Coulomb criterion. However, the admissible candidates located on the feasible domain surface, must be adjusted to comply with the Drucker–Prager criterion

$$\operatorname{tr}(\dot{\varepsilon}) \geqslant \sqrt{\frac{2\sin^2\phi}{3+\sin^2\phi}\left(3\operatorname{tr}(\dot{\varepsilon}^2) - \operatorname{tr}^2(\dot{\varepsilon})\right)} \tag{D1}$$

hence, the points given by (C3a)–(C3d) are replaced by

$$\tilde{e}^1 = \{0, 0, 0\}^{\mathrm{T}} \tag{D2a}$$

$$\tilde{e}^2 = \left\{ \begin{array}{l} w(-rm + 2s_{\mathrm{I}} - s_{\mathrm{II}} - s_{\mathrm{III}}) \\ w(-rm + 2s_{\mathrm{II}} - s_{\mathrm{I}} - s_{\mathrm{III}}) \\ w(-rm + 2s_{\mathrm{III}} - s_{\mathrm{I}} - s_{\mathrm{II}}) \end{array} \right\} \tag{D2b}$$

where

$$m = -\frac{1}{r}\sqrt{\frac{2\sin^2(\phi)}{3+\sin^2(\phi)}a}, \quad w = \frac{rm\left(3\dfrac{c}{\tan(\phi)} - s_{\mathrm{I}} - s_{\mathrm{II}} - s_{\mathrm{III}}\right) + a}{3r((rm)^2 + a)}$$

$$a = 2(\tilde{s}^{\mathrm{T}}\tilde{s} - s_{\mathrm{I}}s_{\mathrm{II}} - s_{\mathrm{I}}s_{\mathrm{III}} - s_{\mathrm{II}}s_{\mathrm{III}})$$

D.2. 2D plane strain problems

For 2D plane strain problems, this criterion coincides with the Mohr–Coulomb one.

REFERENCES

1. Sloan SW, Kleeman PW. Upper bound limit analysis using discontinuous velocity fields. *Computer Methods in Applied Mechanics and Engineering* 1995; **127**:293–314.
2. Christiansen E. Limit analysis of collapse states. In *Handbook of Numerical Analysis* (*Part* 2), Ciarlet PG, Lions JL (eds), vol. IV. North-Holland: Amsterdam, 1996; 193–312.
3. Pastor J, Thai T-H, Francescato P. Interior point optimization and limit analysis: an application. *Communications in Numerical Methods in Engineering* 2003; **19**(10):779–785.
4. Zouain N, Herskovits J, Borges LA, Feijóo RA. An iterative algorithm for limit analysis with nonlinear yield functions. *International Journal of Solids and Structures* 1993; **30**:1397–1417.
5. Christiansen E, Andersen KD. Computation of collapse states with von Mises type yield condition. *International Journal for Numerical Methods in Engineering* 1999; **46**(8):1185–1202.
6. Lyamin AV, Sloan SW. Lower bound limit analysis using non-linear programming. *International Journal for Numerical Methods in Engineering* 2002; **55**:573–611.
7. Lyamin AV, Sloan SW. Upper bound limit analysis using linear finite elements and non-linear programming. *International Journal for Numerical and Analytical Methods in Geomechanics* 2002; **26**:181–216.
8. Li HX, Yu HS. Kinematic limit analysis of frictional materials using nonlinear programming. *International Journal of Solids and Structures* 2005; **42**:4058–4076.

DOI: 10.1002/nme

9. Hill R. *The Mathematical Theory of Plasticity*. The Oxford Engineering Science Series. Clarendon Press: Oxford, 1950.
10. Salençon J. *De l'élasto-plasticité au calcul à la rupture* (1st edn). Les éditions de l'école Polytechnique: Paris, 2002.
11. Zienkiewicz OC, Taylor RL. *The Finite Element Method*, *Volume 1—Basic Formulation and Linear Problems* (4th edn). McGraw-Hill: New York, 1997.
12. Nocedal J, Wright SJ. *Numerical Optimization*. Springer Series in Operations Research. Springer: New York, copyright 1999.
13. Glowinski R, Le Tallec P. *Augmented Lagrangian and Operator-Splitting Methods in Nonlinear Mechanics*. SIAM: Philadelphia, 1989.
14. Makrodimopoulos A, Martin CM. Upper bound limit analysis using simplex strain elements and second-order cone programming. *International Journal for Numerical and Analytical Methods in Geomechanics* 2007; **31**(6):835–865.
15. Le Tallec P. Numerical solution of viscoplastic flow problems by augmented Lagrangians. *IMA Journal of Numerical Analysis* 1986; **16**(2):185–219.
16. de Borst R, Groen EA. Some observations on element performance in isochoric and dilatant plastic flow. *International Journal for Numerical Methods in Engineering* 1995; **38**:2887–2906.
17. Nagtegaal JC, Parks DM, Rice JR. On numerically accurate finite element solutions in the fully plastic range. *Computer Methods in Applied Mechanics and Engineering* 1974; **4**:153–177.
18. XYZ Scientific Applications, Inc. *TrueGrid 2.2.2 Manual*. XYZ Scientific Applications, Inc., 2005.
19. Prandtl L. Über die härte plastischer körper. *Nachrichten von der Königlichen Gesellschaft der Wissenschaften zu Göttingen*, *Mathematisch-Physikalische Klasse* 1920; **12**:74–85.
20. Tin-Loi F, Ngo NS. Performance of the *p*-version finite element method for limit analysis. *International Journal of Mechanical Sciences* 2003; **45**:1149–1166.
21. Capsoni A. A mixed finite element model for plane strain limit analysis computations. *Communications in Numerical Methods in Engineering* 1999; **15**:101–112.
22. Capsoni A, Corradi L. A finite element formulation of the rigid-plastic limit analysis problem. *International Journal for Numerical Methods in Engineering* 1997; **40**(11):2063–2086.
23. Prager W. *An Introduction to Plasticity*. Addison-Wesley: Reading, MA, 1959.
24. Borges L, Zouain N, Costa C, Feijóo R. An adaptive approach to limit analysis. *International Journal of Solids and Structures* 2001; **38**(10–13):1707–1720.
25. Christiansen E, Pedersen OS. Automatic mesh refinement in limit analysis. *International Journal for Numerical Methods in Engineering* 2001; **50**(6):1331–1346.
26. Lyamin AV, Krabbenhøft K, Sloan SW, Hjiaj M. An adaptative algorithm for upper bound limit analysis using discontinuous velocity fields. In *Proceedings of the ECCOMAS 2004*, *European Congress on Computational Methods in Applied Sciences and Engineering*, Jyväskylä, Finland, Neittaanmäki P, Rossi T, Korotov S, Oñate E, Périaux J, Knörzer D (eds), July 2004.
27. Gaydon FA, McCrum AW. A theoretical investigation of the yield-point loading of a square plate with a central circular hole. *Journal of Mechanics and Physics of Solids* 1954; **2**:156–169.
28. Heitzer M, Staat M. Basis reduction technique for limit and shakedown problems. *Numerical Methods for Limit and Shakedown Analysis*, *Deterministic and Probabilistic Problems*, NIC Series, vol. 15. John von Neuman Institute for Computing (NIC), 2002; 1–51. ISBN 3-00-010001-6
29. Groß-Weege J. On the numerical assessment of the safety factor of elastic–plastic structures under variable loading. *International Journal of Mechanical Sciences* 1997; **39**(4):417–433.
30. Liu Y, Zhang X, Cen Z. Numerical determination of limit loads of three-dimensional structures using boundary element method. *European Journal of Mechanics – A/Solids* 2004; **23**:127–138.
31. Cox AD, Eason G, Hopkins HG. Axially symmetric plastic deformation in soils. *Philosophical Transactions of Royal Society of London*, *Series A Mathematical and Physical Sciences* 1961; **254**(1036):1–45.
32. Krabbenhøft K, Lyamin A, Hjiaj M, Sloan SW. A new discontinuous upper bound limit analysis formulation. *International Journal for Numerical Methods in Engineering* 2005; **63**:1069–1088.
33. Antão A. Analyse de la stabilité des ouvrages souterrains par une méthode cinématique régularisée. *Ph.D. Thesis*, École Nationale des Ponts et Chaussées, July 1997.